

Optically Controlled Topological Phases in the Deformed α - T_3 Lattice

O. Benhaida^{1,2}, E. H. Saidi^{1,2,3}, L. B. Drissi^{1,2,3,*1}

¹*LPHE, Modeling and Simulations, Faculty of Science,
Mohammed V University in Rabat, Rabat, Morocco*

²*CPM, Centre of Physics and Mathematics, Faculty of Science,
Mohammed V University in Rabat, Rabat, Morocco*

³*College of Physical and Chemical Sciences, Hassan II Academy
of Sciences and Technology, Rabat, Morocco.*

(Dated: March 31, 2025)

Haldane's tight-binding model, which describes a Chern insulator in a two-dimensional hexagonal lattice, exhibits quantum Hall conductivity without an external magnetic field. Here, we explore an $\alpha - T_3$ lattice subjected to circularly polarized off-resonance light. This lattice, composed of two sublattices (A and B) and a central site (C) per unit cell, undergoes deformation by varying the hopping parameter γ_1 while keeping $\gamma_2 = \gamma_3 = \gamma$. Analytical expressions for quasi-energies in the first Brillouin zone reveal significant effects of symmetry breaking. Circularly polarized light lifts the degeneracy of Dirac points, shifting the cones from M. This deformation evolves with γ_1 , breaking symmetry at $\gamma_1 = 2\gamma$, as observed in Berry curvature diagrams. In the standard case ($\gamma_1 = \gamma$), particle-hole and inversion symmetries are preserved for $\alpha = 0$ and $\alpha = 1$. The system transitions from a semi-metal to a Chern insulator, with band-specific Chern numbers: $C_2 = 1$, $C_1 = 0$, and $C_0 = -1$ for $\alpha < 1/\sqrt{2}$, shifting to $C_2 = 2$, $C_1 = 0$, and $C_0 = -2$ when $\alpha \geq 1/\sqrt{2}$. For $\gamma_1 > 2\gamma$, the system enters a trivial insulating phase. These transitions, confirmed via Wannier charge centers, are accompanied by a diminishing Hall conductivity. Our findings highlight tunable topological phases in $\alpha - T_3$ lattices, driven by light and structural deformation, with promising implications for quantum materials.

Keywords: $\alpha - T_3$ lattices; Off-resonance light; effective Hamiltonian; topological properties; Hall conductivity.

I. INTRODUCTION

Higher-order topological phases have revolutionized our understanding of quantum materials [1, 2], by extending the concept of topology beyond conventional edge or surface states to boundary modes localized at corners or hinges [3]-[6]. These phases represent a profound advancement in the study of topological phenomena, challenging traditional classifications based on symmetry and topology [7, 8]. This framework builds upon earlier discoveries such as the quantum Hall effect [9, 10], where quantized Hall conductivity is governed by topological invariants like the Chern number [11, 12]. Haldane's seminal work on breaking time-reversal symmetry in honeycomb lattices provided a theoretical foundation for understanding these invariants and their role in phase transitions [13], inspiring experimental realizations in diverse geometries and materials including Lieb and Kagome lattices [15, 16], iron-based honeycomb ferromagnetic insulators [17], and electronic and photonic systems [18-21].

Two-dimensional topological insulators are defined by time-reversal symmetry and a \mathbb{Z}_2 topological invariant [22, 23]. Breaking this symmetry triggers a topological phase transition, forming a Chern insulator characterized by chiral edge states and the quantized Hall effect [24]. The Chern number determines the system's topological phase, with zero indicating a trivial phase. Additionally, circularly polarized off-resonant light can induce topological transitions [25], driving systems from trivial to non-trivial phases through Floquet theory [26, 27]. Second-order photon processes allow for band gap tuning, enabling effective Hamiltonians dependent on light frequency and intensity, as in the Haldane model. This framework explains transitions like the polarized light-induced transition of semi-metallic graphene into a Chern insulator [28]. Such prominent example under non-resonant polarized light involves a phenomenon corroborated by numerous analogous experiments on radiative systems [29, 30].

While most Chern insulators have a Chern number of 1, research is increasingly focused on higher Chern numbers, which have been observed experimentally in systems like thin film magnetic topological insulators and photonic crystals [31]. It has been also predicted theoretically in the Dirac-Weyl semimetals on the $\alpha - T_3$ lattice [32]. Numerous studies have revealed remarkable properties of the $\alpha - T_3$ system, including enhanced Hall conductivity and unconventional Berry phase effects, which are closely tied to its unique electronic structure [33, 34]. For instance, the $\alpha - T_3$ lattice, characterized by a tunable parameter controlling the weight of its flat band, exhibits intriguing phenomena like Klein tunneling and Fabry-Perot resonances, which have been extensively studied in both single-layer and bilayer configurations [33, 34]. Additionally, the interplay between the flat band and the Berry phase in these systems leads to novel magneto-optical properties and phase transitions, such as the quantum spin Hall phase transition [35]. Further insights have been gained from detailed analyses of Floquet states in optically driven $\alpha - T_3$

lattices. Under resonant and circularly polarized light irradiation, these systems exhibit the opening of Berry phase-dependent optical gaps, revealing unique topological signatures and symmetry-driven phenomena [36]. Moreover, the dice lattice, a special case of the $\alpha - T_3$ model with a flat band parameter, has shown to exhibit higher Chern numbers, accompanied by a significant enhancement in unconventional Hall conductivity [37].

High Chern numbers have also been reported in decorated lattices, multi-orbital systems, and lattices with spin-orbit coupling or ultracold gases, broadening the understanding of topological materials. Introducing the Haldane model into a bilayer of the $\alpha - T_3$ lattice has resulted in observed Chern numbers of up to 5 [38], along with a substantial enhancement of the $6e^2/h$ Hall conductivity [38, 39]. Other lattice structures, such as the decorated honeycomb or starlike lattices [40], and multi-orbital triangular lattices [41], also exhibit high Chern numbers and larger jumps. High Chern numbers have also been reported in Dirac [42] and semi-Dirac [43] systems. Additionally, the presence of spin-orbit coupling in honeycomb lattices [44] and ultracold gases in triangular lattices [45] has been shown to give rise to high Chern numbers. These studies contribute to a deeper understanding of the topological properties of these advanced materials.

In this work, we explore the topological properties of the $\alpha - T_3$ lattice, a fascinating system that generalizes the honeycomb lattice. The $\alpha - T_3$ lattice consists of two sublattices, A and B, representing carbon atoms located at the vertices of a hexagonal structure, and a third site, C, positioned at the center of each hexagon, as illustrated in Fig. 1. Within this structure, quasiparticles can hop from site C to site A within the same hexagon. The hopping energy between sites A and B is described as $\gamma \cos \phi$, while that between sites A and C is $\gamma \sin \phi$. The parameter α , defined by $\tan \phi = \alpha$, governs the lattice configuration. By varying α between 0 and 1, different lattice structures can be realized: when $\phi = 0$ ($\alpha = 0$), the lattice corresponds to graphene, and when $\phi = \pi/4$ ($\alpha = 1$), it becomes the dice lattice. Further details about this lattice structure are provided in [46].

In this study, we investigate the topological properties of the $\alpha - T_3$ lattice under the influence of an external off-resonant electric field. This field induces a term analogous to the Haldane model, breaking time-reversal symmetry and modulating the band gap, which is pivotal in determining the system's topological properties. The simultaneous tunability of the α parameter and the presence of a flat band create a distinctive energy dispersion. Additionally, we consider the effect of anisotropic deformations by altering the hopping energies of quasiparticles between nearest-neighbor bonds. Specifically, the hopping energy along the position vector δ_1 changes to $\gamma_1 \sin \phi$ for sites A and C, and $\gamma_1 \cos \phi$ for sites A and B, while the hopping energies along vectors δ_2 and δ_3 remain unchanged. As the parameter γ_1 increases, the Dirac points approach each other and eventually merge at the M point in the Brillouin zone when $\gamma_1 = 2\gamma$, leading to band closure and the loss of topological properties. This critical point marks a topological phase transition. Beyond this point, the energy dispersion acquires a Dirac-like form along the k_x -axis, a phenomenon that has been previously observed in graphene [47], graphene bilayers [48], and the dice lattice [49]. Furthermore, this method has been applied to the single-layer honeycomb structure Si_2O , yielding a semi-Dirac dispersion [50].

To gain deeper insights, we study the effects of deformation on the topological properties by tuning the hopping energy γ_1 to specific values. We calculate the Berry curvature, which encapsulates key symmetries such as particle-hole symmetry, inversion symmetry, and C_3 symmetry in the standard case ($\gamma_1 = \gamma$). As γ_1 deviates from γ , the C_3 symmetry is broken, leading to topological transitions. We also compute the Chern number, which indicates the system's transition from a non-trivial to a trivial topological phase. To further confirm this transition, we analyze the evolution of the Wannier charge center along a closed loop in the Brillouin zone, representing the average charge position within the unit cell. This analysis is consistent with the behavior of surface energy bands [51–53]. Moreover, we investigate the quantum Hall conductivity and its response to the deformation of the energy spectrum as γ_1 varies. Our results provide valuable insights into the interplay between lattice deformation and topological phase transitions, shedding light on the tunable nature of topological properties in $\alpha - T_3$ lattices.

The originality of the present work lies in its comprehensive analysis of the interplay between lattice deformation, external electric fields, and topological properties in the $\alpha - T_3$ lattice. By exploring the combined effects of anisotropic hopping energies, Berry curvature, and quantum Hall conductivity, this study not only advances the understanding of topological materials but also paves the way for potential applications in quantum technologies.

This article is organized as follows: Section II presents the Hamiltonian describing quasiparticle dynamics in irradiated and deformed $\alpha - T_3$ lattices. Section III analyzes and discusses the quasi-energy spectrum. Section IV investigates the topological properties of this lattice, including the Berry curvature (Subsection IV A), the Chern phase diagram (Subsection IV B), and the evolution of the Wannier charge center (Subsection IV C). Section V examines the anomalous Hall conductivity. Finally, Section VI provides a conclusion and summary of the work.

II. MODEL AND HAMILTONIAN

The rescaled tight-binding Hamiltonian describing the motion of a quasiparticle along a p_z orbital in a $\alpha-T_3$ lattice between its nearest neighbours is given by [46]

$$H(\mathbf{k}) = \begin{pmatrix} 0 & \cos(\varphi)\rho(\mathbf{k}) & 0 \\ \cos(\varphi)\rho^*(\mathbf{k}) & 0 & \sin(\varphi)\rho(\mathbf{k}) \\ 0 & \sin(\varphi)\rho^*(\mathbf{k}) & 0 \end{pmatrix} \quad (1)$$

where $\rho(\mathbf{k}) = \sum_{j=1}^3 \gamma_j e^{i\mathbf{k}\delta_j}$ and δ_j are the vectors connecting the nearest neighbors, and γ_j is the hopping energy. In our model, we consider γ_1 along the $\delta_1 = a(0, 1)$ direction and $\gamma_2 = \gamma$, $\gamma_3 = \gamma$ along the $\delta_2 = a(-\sqrt{3}/2, -1/2)$ and $\delta_3 = a(\sqrt{3}/2, -1/2)$ directions where a is the distance of the nearest neighbour, as shown in Fig.1. In this section we'll study photon-electron interactions by applying a polarised electric field perpendicular to the plane of the $\alpha-T_3$ lattice. The electric field is derived from the vector potential with respect to time $\partial_t A(t)$, and this vector potential depends on time, $\mathbf{A}(t) = A_0(\sin(\omega t), \cos(\omega t))$, where ω and A_0 are the radiation frequency and the vector potential amplitude, respectively. The intensity of light is characterized by a dimensionless parameter $\varsigma = eA_0a_0/\hbar$ and is much smaller than 1, where $a_0 = \sqrt{3}a$ and e is the electric charge.

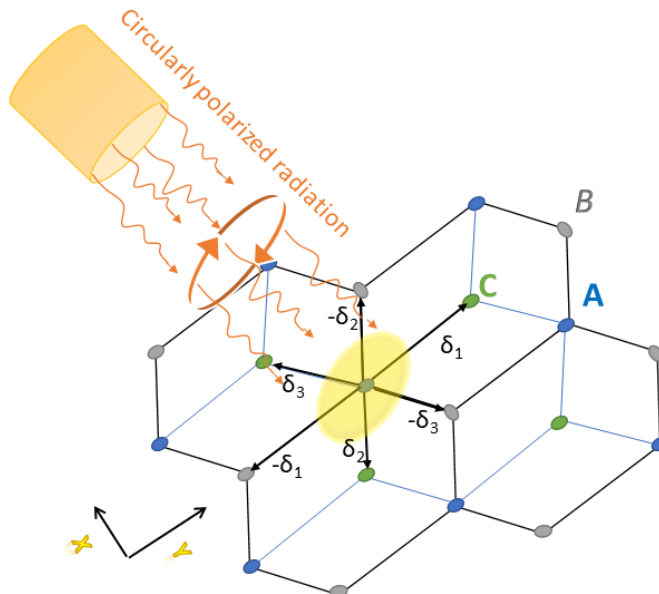


FIG. 1. Schematic of a deformed $\alpha-T_3$ lattice exposed to circularly polarized off-resonance light, where the deformation affects only the position vector δ_1 , changing the hopping energy from $\gamma_1 = \gamma$ to 2.5γ , while the hopping energies $\gamma_1 = \gamma$ and $\gamma_2 = \gamma$ associated with the position vectors δ_2 and δ_3 remain unchanged.

when an electric field is applied to electrons moving from site \mathbf{m} to the nearest site $\mathbf{m} + \delta$, they gain energy, represented by the hopping energy γ_j , which is transformed into $\gamma_j e^{i\varpi}$, where $\varpi = e/\hbar \int_{\mathbf{m}}^{\mathbf{m}+\delta} \mathbf{A}(t) d\mathbf{x}$ is the phase factor gained by the electron. The Hamiltonian then becomes

$$H(\mathbf{k}, t) = \begin{pmatrix} 0 & \cos(\varphi)\rho(\mathbf{k}, t) & 0 \\ \cos(\varphi)\rho^*(\mathbf{k}, t) & 0 & \sin(\varphi)\rho(\mathbf{k}, t) \\ 0 & \sin(\varphi)\rho^*(\mathbf{k}, t) & 0 \end{pmatrix}, \quad (2)$$

with $\rho(\mathbf{k}, t) = \sum_{j=1}^3 \gamma_j e^{i(\mathbf{k}+e\mathbf{A}(t))\delta_j} = \sum_{n=0}^{\infty} J_n(\varsigma) [\gamma_1 e^{in\omega t} e^{i\mathbf{k}\delta_1} + \gamma e^{i\mathbf{k}\delta_2} e^{-in(\omega t + \pi/3)} + \gamma e^{i\mathbf{k}\delta_3} e^{in(\pi/3 - \omega t)}]$, where $J_n(\varsigma)$ is a Bessel function of the first kind. We consider that the light incident on the $\alpha-T_3$ lattice has an off-resonance frequency, as explained in [25]. When an electron is subjected to an off-resonance frequency, it does not excite it directly but simply modifies the band structure in an effective way by absorbing and emitting virtual photons. An off-resonance state is reached when the frequency of the photons is well above the bandwidth, i.e. $\omega \gg 3\gamma_1$. We have a time-dependent and periodic Hamiltonian $H(T+t, \mathbf{k}) = H(t, \mathbf{k})$. Floquet's theorem is perhaps the most

convenient solution to this problem, with $T = 2\pi/\omega$. In this case, we can describe the properties of the off-resonance light effect by means of the effective Hamiltonian [25, 39].

$$H_{eff}(\mathbf{k}) = H_0(\mathbf{k}) + \frac{1}{\hbar\omega} [H_{-1}(\mathbf{k}), H_{+1}(\mathbf{k})] + \epsilon(1/\omega^2). \quad (3)$$

We express the time-dependent Fourier components of the Hamiltonian as follows:

$$H_s(\mathbf{k}) = \frac{1}{T} \int_0^T H(\mathbf{k}, t) e^{-iswt} dt. \quad (4)$$

The second term is responsible for the absorption of a virtual photon by an electron through $H_1 H_{-1}$ and its emission through $H_{-1} H_1$. We give the explicit expression of the effective Hamiltonian considering terms up to $\epsilon(1/\omega)$.

$$H_{eff}(\mathbf{k}) = \begin{pmatrix} \eta(\mathbf{k}) \cos(\varphi)^2 & J_0(\varsigma) \cos(\varphi) \rho(\mathbf{k}) & 0 \\ J_0(\varsigma) \cos(\varphi) \rho^*(\mathbf{k}) & -\eta(\mathbf{k}) \cos(2\varphi) & J_0(\varsigma) \sin(\varphi) \rho(\mathbf{k}) \\ 0 & J_0(\varsigma) \sin(\varphi) \rho^*(\mathbf{k}) & -\eta(\mathbf{k}) \sin(\varphi)^2 \end{pmatrix}, \quad (5)$$

and $\eta(\mathbf{k})$ are defined as follows

$$\eta(\mathbf{k}) = 2\Delta \left(-\cos\left[\frac{\sqrt{3}k_x a}{2}\right] + \frac{\gamma_1}{\gamma} \cos\left(\frac{3k_y a}{2}\right) \right) \sin\left(\frac{\sqrt{3}k_x a}{2}\right). \quad (6)$$

where $\Delta = \frac{\sqrt{3}\gamma^2\varsigma^2}{2\hbar\omega}$. We consider a weak conduit $\varsigma \ll 1$, which implies taking the approximation $J_0(\varsigma) \approx 1$ and $J_1(\varsigma) \approx \frac{\varsigma}{2}$. $\eta(\mathbf{k})$ is the light-induced term, identical to the near-second Haldane term with $\phi = \pi/2$ and $t_2 = \Delta$, which satisfies the Haldane model for graphene and the dice lattice [37, 47]. This term is responsible for breaking the time reversal symmetry. This results in a gap in the Dirac points. Later we'll discuss the γ_1 -effect, which is a mesh distortion that changes the location of this gap.

As explained previously [32], if we take $\gamma_1 = \gamma$, $H_{eff}(\mathbf{k})$ satisfies the anticommutation relations when $\alpha = 0$ and $\alpha = 1$.

$$\{H_{eff}^{\alpha=0}(\mathbf{k}), C^{\alpha=0}\} = 0, \quad \{H_{eff}^{\alpha=1}(\mathbf{k}), C^{\alpha=1}\} = 0. \quad (7)$$

where $C^{\alpha=0}$ is defined as the graphene operator and $C^{\alpha=1}$ as the dice operator, given as:

$$C^{\alpha=0} \begin{pmatrix} 0 & -1 & 0 \\ 1 & 0 & 0 \\ 0 & 0 & 1 \end{pmatrix} \mathcal{K}, \quad C^{\alpha=1} \begin{pmatrix} 0 & 0 & -1 \\ 0 & 1 & 0 \\ -1 & 0 & 0 \end{pmatrix} \mathcal{K}. \quad (8)$$

with \mathcal{K} as the complex conjugate, equation (7) implies the existence of a particle and a hole such that $\varepsilon(\mathbf{k}) = -\varepsilon(-\mathbf{k})$, as well as a flat band at zero. However, when we take $\gamma_1 = 2\gamma$ and whatever α is, at point \mathbf{M} (see Fig.2), $H_{eff}(\mathbf{k})$ satisfies the anticommutation relations.

$$\{H_{eff}(\mathbf{k}), C^{\alpha=0}\} = 0, \quad \{H_{eff}(\mathbf{k}), C^{\alpha=1}\} = 0. \quad (9)$$

In this case, we can conclude that the radiation does not affect the system in the same way as it would normally, because the system no longer depends on α . We will later demonstrate the importance of modifying γ_1 , as this results in the deformation of a lattice, a change γ_1 , and an observation of its effect on topological properties.

III. QUASIENERGY AND BAND STRUCTURE

In this section, we study the energy bands as γ_1 varies. The Hamiltonian will be diagonalized to obtain the eigenvalues. This diagonalization leads to the characteristic equation, known as the *depressed cubic equation*, $\lambda_3\varepsilon^3 + \lambda_1\varepsilon + \lambda_0 = 0$, whose solutions can be expressed as follows:

$$\varepsilon_\nu(\mathbf{k}) = 2\sqrt{\frac{-\lambda_1}{3}} \cos \left[\frac{1}{3} \arccos \left[\frac{3\lambda_0}{2\lambda_1} \sqrt{\frac{-3}{\lambda_1}} \right] - \frac{2\nu\pi}{3} \right], \quad (10)$$

and

$$\lambda_0 = -\frac{1}{8}\eta^3(\mathbf{k}) \sin(2\varphi) \sin(4\varphi), \quad (11)$$

$$\lambda_1 = -\frac{1}{8} (8|\rho(\mathbf{k})|^2 + \eta^2(\mathbf{k})(5 + 3 \cos(4\phi))), \quad (12)$$

$$\lambda_3 = 1. \quad (13)$$

The quasi-energy associated with the conduction band is represented by the value $\nu = 0$, while the flat band and the valence band are represented by the values $\nu = 1$ and $\nu = 2$, respectively. These quasienergies correspond to normalised pseudo-vectors.

$$|\Upsilon_\nu(\mathbf{k})\rangle = \mathcal{N}_\nu(\mathbf{k}) \begin{pmatrix} -\frac{\cos(\phi)\rho(\mathbf{k})}{-\varepsilon_\nu(\mathbf{k})+\eta(\mathbf{k})} & 1 \\ \frac{\sin(\phi)\rho^*(\mathbf{k})}{\varepsilon_\nu(\mathbf{k})+\eta(\mathbf{k})} & \end{pmatrix}^T, \quad (14)$$

and

$$\mathcal{N}_\nu(\mathbf{k}) = \left[1 + |\rho(\mathbf{k})|^2 \left(\frac{\cos^2(\phi)}{(-\varepsilon_\nu(\mathbf{k}) + \eta(\mathbf{k}))^2} + \frac{\sin^2(\phi)}{(\varepsilon_\nu(\mathbf{k}) + \eta(\mathbf{k}))^2} \right) \right]^{-1/2}. \quad (15)$$

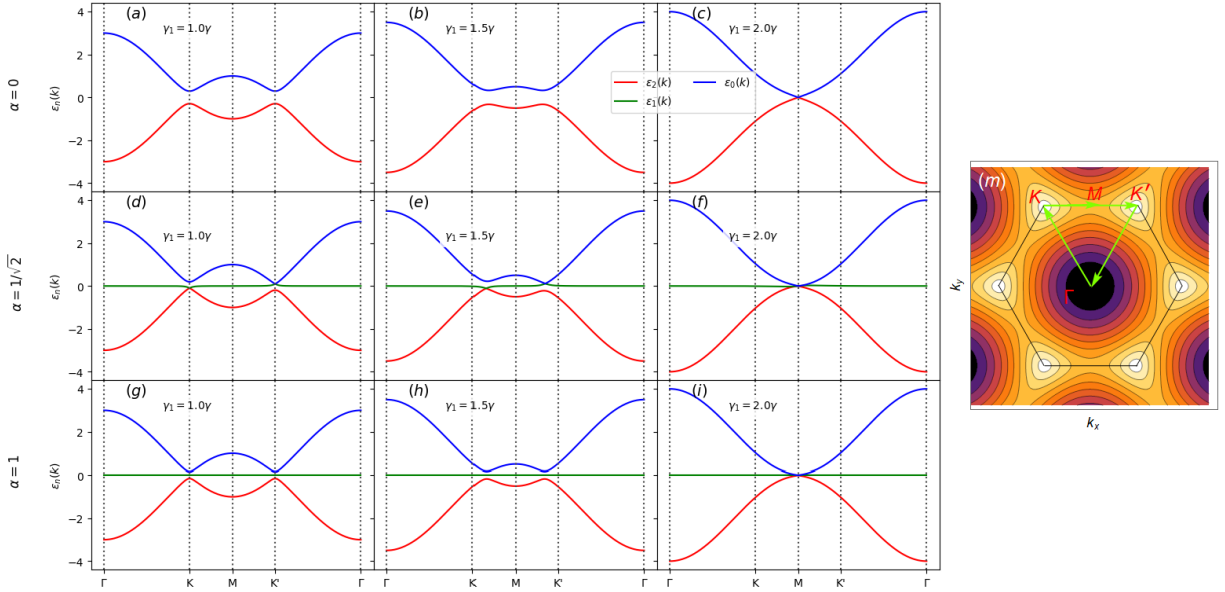


FIG. 2. The band structure of the irradiated and deformed $\alpha - T_3$ lattice is illustrated as a function of $\gamma_1 = \beta\gamma$ along the k_x axis in the following cases: • (a) $\gamma_1 = 1\gamma$, (b) $\gamma_1 = 1.5\gamma$, (c) $\gamma_1 = 2\gamma$, (d) $\gamma_1 = 2.1\gamma$ with $\alpha = 0$, • (e) $\gamma_1 = 1\gamma$, (f) $\gamma_1 = 1.5\gamma$, (g) $\gamma_1 = 2\gamma$, (h) $\gamma_1 = 2.1\gamma$ with $\alpha = \frac{1}{\sqrt{2}}$, • (i) $\gamma_1 = 1\gamma$, (j) $\gamma_1 = 1.5\gamma$, (k) $\gamma_1 = 2\gamma$, (l) $\gamma_1 = 2.1\gamma$ with $\alpha = 1$. Sub-figure (m) represents the first Brillouin zone of the hexagonal lattice used to calculate and structure the band structure along the path ($\Gamma \rightarrow K \rightarrow M \rightarrow K' \rightarrow \Gamma$).

Before discussing the band structure, we determine the path of the first Brillouin zone in the reciprocal lattice, which is in the form of a hexagonal lattice, to construct the band structure path, as shown in Fig.2-(m). Now, we analyse and discuss the band structure by varying α for three values: 0, $1/\sqrt{2}$ and 1. In addition, for each fixed value of α , we vary γ_1 while keeping Δ constant. It is known that when the $\alpha - T_3$ lattice is not exposed to radiation, the three bands touch at the Fermi level at points $\mathbf{K} \left(-\frac{2\pi}{3\sqrt{3}a}, \frac{2\pi}{3a} \right)$ and $\mathbf{K}' \left(\frac{2\pi}{3\sqrt{3}a}, \frac{2\pi}{3a} \right)$, known as Dirac points. On the other hand, under the effect of active radiation, a gap opens that is in a quasi-energy sense dependent on α . As γ_1 increases, we observe that for $\alpha = 0$ (see fig2(a)-2(c)), in the case of graphene, the gap progressively decreases, moving away from the Dirac points and adopting a behaviour similar to the deformed Haldane model. When γ_1 reaches a particular value, $\gamma_1 = 2\gamma$, the gap disappears at the point $\mathbf{M}(0, \frac{2\pi}{3a})$ (see figure 2(c)), where two bands

degenerate. Similar behaviour is observed for dice lattices ($\alpha = 1$), which also have a structure close to the deformed Haldane model. In this case the gap decreases with increasing γ_1 and the conduction, flat, and valence bands become degenerate at the \mathbf{M} point for $\gamma_1 = 2\gamma$ (see fig 2(d)). This happens despite the presence of radiation that breaks the time-reversal symmetry. The spectrum then exhibits a semi-Dirac-type dispersion, characterised by a quadratic dependence along k_x and a linear dependence along k_y , in the absence of radiation. In the presence of radiation, for $\gamma_1 = 2\gamma$, electrons move with distinct and linear velocities in both directions, thereby revealing a linear anisotropy. When γ_1 passes 2γ ($\gamma_1 > 2\gamma$), a gap opens at point \mathbf{M} . For $\alpha = 1/\sqrt{2}$, the gap partially closes at points \mathbf{K} and \mathbf{K}' , as illustrated in Figure 2(i)-(j). At points \mathbf{K} and \mathbf{K}' , the dispersion becomes kinetic, except in the interval $\gamma \leq \gamma_1 < 2\gamma$. Conversely, when $\gamma_1 = 2\gamma$, the gap disappears and the bands become degenerate at point \mathbf{M} . When $\gamma_1 > 2\gamma$, the effect of radiation is unable to control the gap adjustment, leading to a reopening of the gap. In summary, we can conclude that the effect of radiation is significant only in the interval $\gamma \leq \gamma_1 < 2\gamma$.

One aspect that merits attention is that, despite the system being subjected to radiation and γ_1 being fixed at 2γ , the gap closes and the time-reversal symmetry remains broken. This could indicate a change in the topological properties of the $\alpha - T_3$ lattice. This is precisely what we are going to examine in the study of topological properties as γ_1 varies.

IV. TOPOLOGICAL PROPERTIES

In this section, we study the effect of deformation from γ_1 change on Berry curvature, Chern number, and Wannier charge center.

A. Berry curvature

In this subsection we analyze the Berry curvature, which plays a crucial role in topological quantum physics. It is characterized by the operations of the following discrete symmetries: time inversion symmetry $\hat{T}^{-1}\Omega_\nu(\mathbf{k})\hat{T} = -\Omega_\nu(-\mathbf{k})$, charge conjugation symmetry $\hat{C}^{-1}\Omega_\nu(\mathbf{k})\hat{C} = -\Omega_{\bar{\nu}}(-\mathbf{k})$, and inversion symmetry $\hat{I}^{-1}\Omega_\nu(\mathbf{k})\hat{I} = \Omega_\nu(-\mathbf{k})$, where $\bar{\nu}$ represents the quasi-energy index conjugate of ν ($\varepsilon_{\bar{\nu}}(\mathbf{k}) = -\varepsilon_\nu(\mathbf{k})$). We are interested in the effect of the variation of γ_1 on this Berry curvature symmetry. To do this, we numerically calculate the Berry curvature of the system in the z-component, which is given by [54]

$$\Omega_\nu(\mathbf{k}) = -2\Im \sum_{\nu' \neq \nu} \frac{\langle \Upsilon_\nu(\mathbf{k}) | v_x | \Upsilon_{\nu'}(\mathbf{k}) \rangle \langle \Upsilon_{\nu'}(\mathbf{k}) | v_y | \Upsilon_\nu(\mathbf{k}) \rangle}{(\varepsilon_\nu(\mathbf{k}) - \varepsilon_{\nu'}(\mathbf{k}))^2}, \quad (16)$$

where $v_i = \hbar^{-1} \partial_{k_i} H(\mathbf{k})$ is the effective velocity in the axial direction $i = x, y$. We know that the Berry curvature, if not zero, results from the breaking of the time-reversal symmetry, or at least from the presence of a broken symmetry, as mentioned previously. We now plot the Berry curvature to analyze this symmetry and to study the effect of variations of γ_1 . We vary γ_1 in two cases: $\gamma_1 = \gamma$ and $\gamma_1 = 2\gamma$.

For $\gamma_1 = \gamma$, time-reversal symmetry is broken when Berry curvatures differ from zero for any value of alpha and any individual Berry curvature. Charge conjugate symmetry is present for $\alpha = 0$ and 1, see Fig 3 where the Berry curvature $\hat{C}^{-1}\Omega_2(\mathbf{k})\hat{C} = -\Omega_0(-\mathbf{k})$ and the associated curvature of a flat band Ω_1 is zero, and when \mathbf{k} is given, it's clear that the sum of the individual Berry curvatures is zero, so the local conservation of Berry curvature and also the inversion symmetry is present $\hat{I}^{-1}\Omega_2(\mathbf{k})\hat{I} = \Omega_2(-\mathbf{k})$ and $\hat{I}^{-1}\Omega_0(\mathbf{k})\hat{I} = \Omega_0(-\mathbf{k})$, but for $\alpha \neq 0$ and 1 the conjugate charge and inversion symmetry are broken. The expression for the Berry curvature can be found analytically in the case where $\alpha = 1$, and is written like this

$$\Omega_\nu(\mathbf{k}) = \frac{\Theta(\mathbf{k})}{(|\rho(\mathbf{k})|^2 + \eta^2(\mathbf{k})/2)^{3/2}} (\delta_{\nu,0} + 0 * \delta_{\nu,1} - \delta_{\nu,2}), \quad (17)$$

and

$$\begin{aligned} \Theta(\mathbf{k}) = & \frac{\sqrt{3}}{8\gamma} a^2 \Delta \left(3\gamma(\gamma^2 + 2\gamma_1^2) + 4\gamma(\gamma^2 - 2\gamma_1^2) \cos(\sqrt{3}ak_x) + \gamma^3 \cos(2\sqrt{3}ak_x) \right. \\ & + \gamma_1 \left[2(-3\gamma^2 + \gamma_1^2) \cos\left(\frac{1}{2}a(\sqrt{3}k_x - 3k_y)\right) + \gamma\gamma_1 \cos\left(a(\sqrt{3}k_x - 3k_y)\right) \right. \\ & \left. \left. + 2(-3\gamma^2 + \gamma_1^2) \cos\left(\frac{1}{2}a(\sqrt{3}k_x + 3k_y)\right) + \gamma\gamma_1 \cos\left(a(\sqrt{3}k_x + 3k_y)\right) \right] \right). \end{aligned} \quad (18)$$

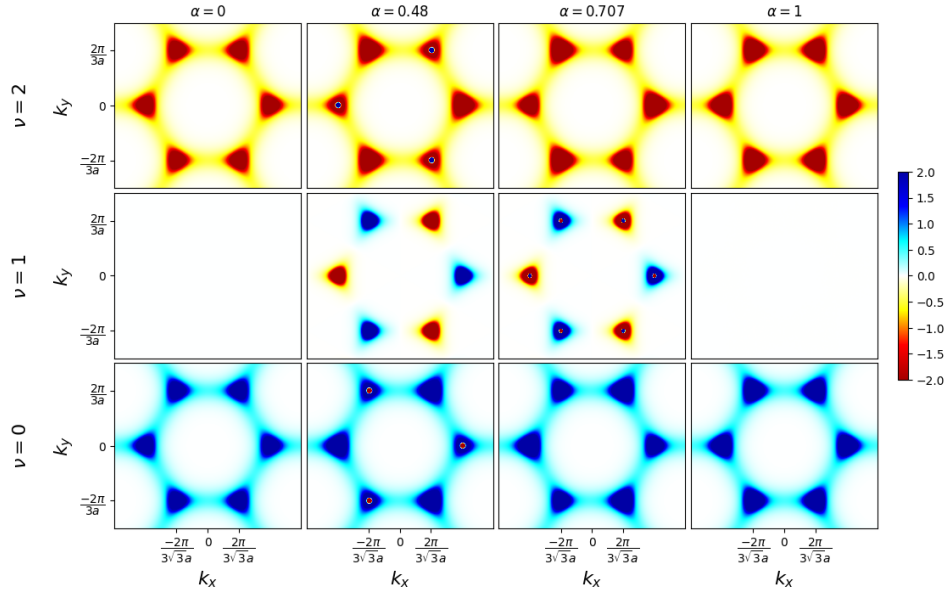


FIG. 3. The Berry curvature distribution in the $k_x - k_y$ plane, corresponding to the conduction ($\nu = 0$), flat ($\nu = 1$) and valence ($\nu = 2$) bands, is calculated for different values of parameter α : $\alpha = 0$ (the graphene case), $\alpha = 0.48$, $\alpha = 1/\sqrt{2}$ (critical value corresponding to the phase transition where the band becomes dispersive at the Dirac point, as illustrated in Fig.2-(d)), and $\alpha = 1$ (dice lattice limit). Calculations are performed by setting $\delta = 0.18\gamma$ in the standard case where $\gamma_1 = 1\gamma$, without any deformation.

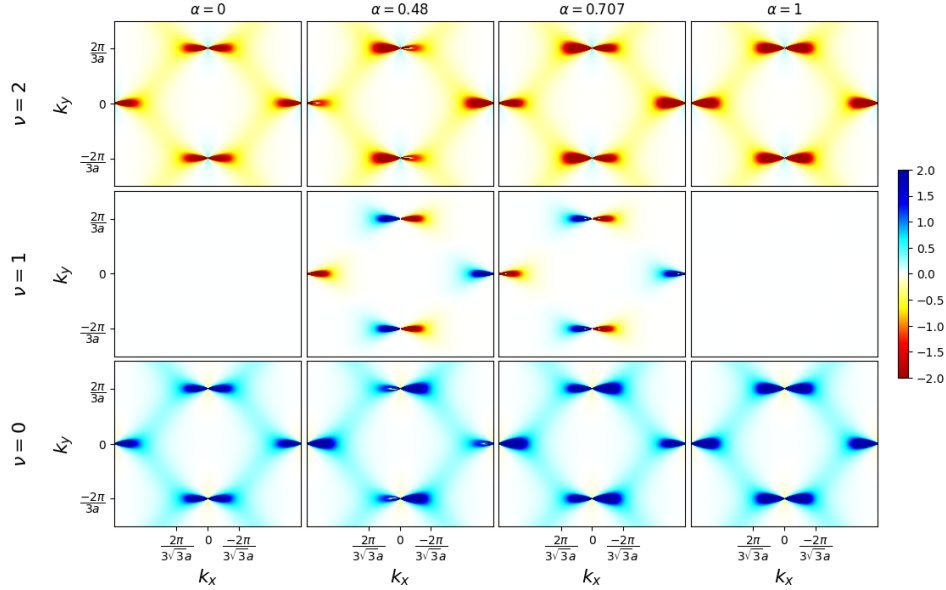


FIG. 4. The Berry curvature distribution in the presence of deformation by modifying $\gamma_1 = 2\gamma$, while maintaining the other parameters in Fig.3.

As we saw previously, the Berry curvature is concentrated at Dirac points \mathbf{K} and \mathbf{K}' for $\gamma_1 = \gamma$ in the Brillouin zone (BZ). As γ_1 increases, we observe that the Berry curvature moves slowly towards point \mathbf{M} for $\gamma_1 = 2\gamma$ (see Fig.4). However, this figure does not include results for other values of γ_1 . The Berry curvature becomes singular at $t_1 = 2\gamma$, where quasi-energy is degenerate at point \mathbf{M} . When we vary γ_1 , the system breaks the inversion symmetry and, more precisely, the C_3 symmetry is also broken in the cases where $\alpha = 0$ and $\alpha = 1$ (see Fig.4).

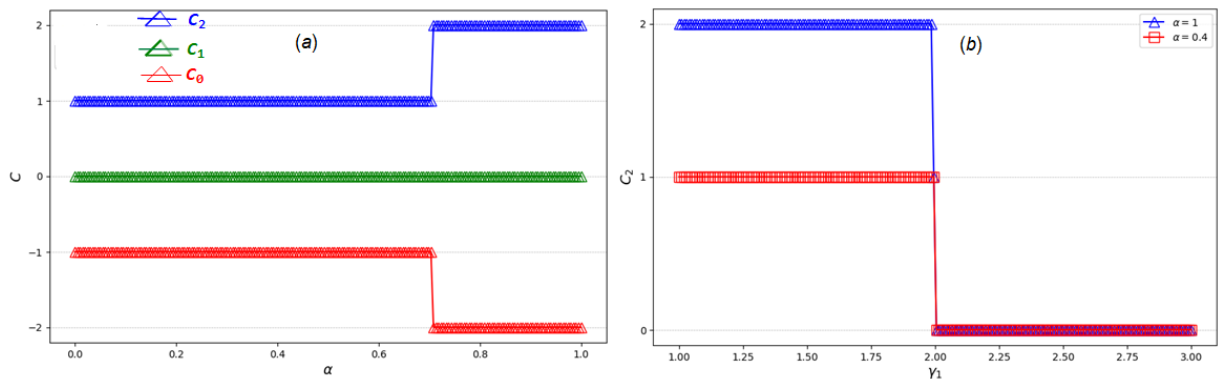


FIG. 5. The variation of the Chern number as a function of the parameters α and γ_1 : For (a) The variation of the Chern number corresponding to the valence ($\nu = 2$), flat ($\nu = 1$) and conduction ($\nu = 0$) bands is shown as a function of α , as illustrated in the figure above. In (b), the variation of the Chern number corresponding to the valence band ($\nu = 2$) as a function of γ_1 is presented. This represents the deformation of the system for $\alpha = 0.4$ and $\alpha = 1$. In all the calculations presented here, we have fixed the parameter $\Delta = 0.18\gamma$.

B. Chern phase diagrams

In this subsection, we aim to obtain the phase diagram of the Chern number. As we have previously mentioned, light induces a term similar to Haldane's term for $\phi = \frac{\pi}{2}$, which is responsible for breaking the time-reversal symmetry. This term, as we have studied, generates a non-zero Berry curvature, which is concentrated at the Dirac points due to the opening of a gap caused by light. This implies the existence of a phase transition, which can be observed through the surface integral of the Berry curvature over the BZ. This integral gives an integer, called the Chern number for the ν -th band, which is defined by the following relationship [54].

$$C_\nu = \frac{1}{2\pi} \int \int_{BZ} \Omega_\nu(\mathbf{k}) d^2\mathbf{k}. \quad (19)$$

Before discussing the evolution of the Chern number as a function of parameter variations, we first consider the standard case where no deformation varies the hopping energy γ_1 , i.e. $\gamma_1 = \gamma$. In the $\alpha - T_3$ lattice there are three bands: two dispersive bands (ε_0 and ε_2) and a flat band (ε_1), which becomes dispersive at the Dirac point when $\alpha = 1/\sqrt{2}$. To observe the topological evolution of the system, we study the transition between the graphene lattice ($\alpha = 0$) and the dice lattice limit ($\alpha = 1$), varying α from 0 to 1. The system becomes topologically non-trivial due to a non-zero Chern number, except for the Chern numbers associated with the bands $\nu = 0$ and $\nu = 2$. We see that there is a phase transition at $\alpha = 1/\sqrt{2}$, where the Chern numbers of the bands are $C_2(C_0) = 1(-1)$ in the range $0 \leq \alpha < 1/\sqrt{2}$. At $\alpha = 1/\sqrt{2}$ these values change from $C_2(C_0) = 1(-1)$ to $C_2(C_0) = 2(-2)$ when $1/\sqrt{2} \leq \alpha \leq 1$ (see Fig.5-(a)). On the other hand, the Chern number associated with the band $\nu = 1$ remains zero, indicating that it is topologically trivial. We now consider the $\alpha - T_3$ lattice irradiated and deformed along the displacement vector δ_1 , resulting in a change in the hopping energy γ_1 . For this study we choose a variation region of γ_1 between $[\gamma, 3\gamma]$. We investigate the evolution of the Chern number C_2 , which is the inverse of C_0 , while C_1 remains topologically trivial. Fixing $\Delta = 0.2\gamma$ and $\alpha = 0.4$ as well as $\gamma = 1$, we plot C_2 as a function of γ_1 . For $\gamma_1 = g$, the Chern number C_2 is initially equal to 1 for $\alpha = 0.4$ and 2 for $\alpha = 1$, as shown in Fig.5-(a). As γ_1 increases from g to $\gamma_1 < 2\gamma$, C_2 remains constant regardless of the value of α . However, as γ_1 exceeds 2γ , the system undergoes a change in topological properties from a topologically non-trivial to a topologically trivial state. This change, characteristic of a phase transition, occurs precisely at $\gamma_1 = 2\gamma$. As shown in Fig.5-(b), the Chern number C_2 changes from 1 ($\alpha = 0.4$) or 2 ($\alpha = 1$) for $\gamma_1 = \gamma$ to 0 ($\alpha = 0.4$) or 0 ($\alpha = 1$) for $\gamma_1 > 2\gamma$. We also analyze variations in the Chern number C_2 by modifying the parameters Δ/γ and α . To do this, we plot C_2 as a function of these parameters by fixing γ_1 in three cases: $\gamma_1 = 1\gamma, 1.5\gamma$, and 2γ , as illustrated in the topological phase diagram in Fig.6. This diagram highlights the topological phases of the system, represented by different colors: red corresponds to $C_2 = 2$, yellow to $C_2 = 1$, and white indicates a topologically trivial phase with $C_2 = 0$. In the first case, where $\gamma_1 = \gamma$ (see Fig.6-(a)), when the polarization amplitude Δ/γ is initially very low, this keeps the system in a topologically trivial phase with $C_2 = 0$ in the interval $\Delta/\gamma \in [0, 0.025]$. However, when $\Delta/\gamma > 0.025$, the system undergoes a topological phase transition: C_2 goes from 0 to 1 in the interval $\alpha \in [0, 1/\sqrt{2}]$. In the range $\alpha \in [1/\sqrt{2}, 1]$, the Chern number changes from $C_2 = 1$ to $C_2 = 2$ for $\Delta/\gamma = 0.05$, precisely in the interval $\alpha \in [0.85, 1]$. As D increases

further ($\Delta/\gamma > 0.08$), the system reaches a phase where $C_2 = 2$ holds for any value of Δ/γ in the interval $\alpha \in [1/\sqrt{2}, 1]$.

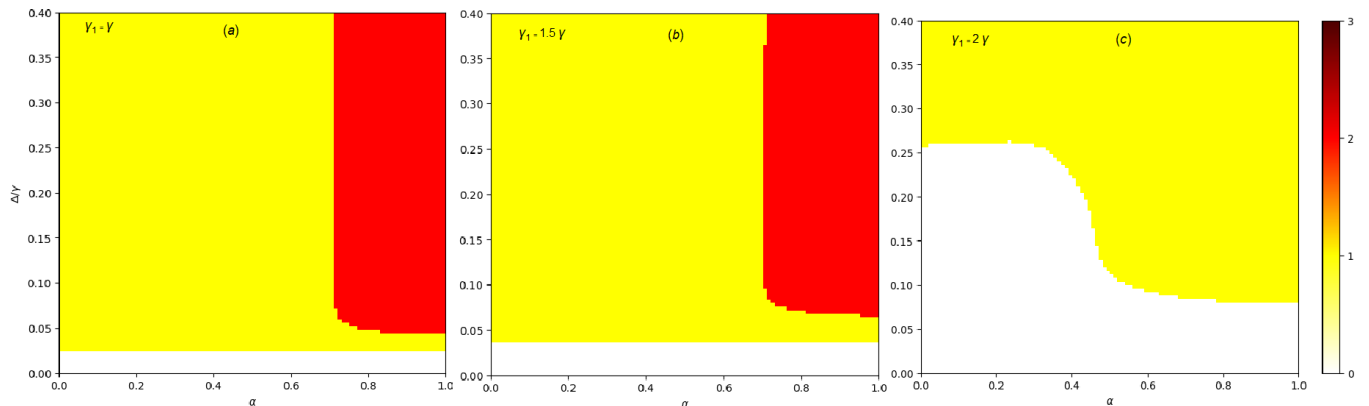


FIG. 6. The phase diagram of the Chern number associated with the valence band ($\nu = 2$) of the irradiated and deformed $\alpha - T_3$ lattice is presented in parameter space ($\Delta/\gamma \in [0, 0.4]$) and ($\alpha \in [0, 1]$). The phase diagram is shown for (a) $\gamma_1 = \gamma$, (b) $\gamma_1 = 1.5\gamma$ and (c) $\gamma_1 = 2\gamma$.

In the second case, by setting $\gamma_1 = 1.5\gamma$, we observe that the system undergoes a topological phase transition. It goes from a non-trivial phase in the interval $\Delta/\gamma \in [0.025, 0.04]$ to a topologically trivial phase. Another phase transition is identified in the interval $\alpha \in [0.85, 1]$, which occurs at $\Delta/\gamma = 0.07$ (see Fig. 6-(b)).

In the third case, when $\gamma_1 = 2\gamma$, the system changes its topological property between $\Delta/\gamma \in [0.05, 0.1]$. It moves from a topologically trivial to a non-trivial phase, unlike the case $\gamma_1 = \gamma$, where the values of $C_2 = 1$ and $C_2 = 2$ are replaced by $C_2 = 0$ (see Fig. 6-(c)). These observations show that varying γ_1 changes the topological properties of the system, moving it from a non-trivial to a trivial state.

To confirm whether or not the system remains in a non-trivial topological insulating state as γ_1 varies, we would like to study the evolution of the Wannier charge center in the next subsection.

C. Wannier charge centers

This subsection focuses on examining Wannier charge centres (WCCs) as a means to observe and analyse topological evolution, a fundamental aspect of the diagnostic process of topological band properties [51, 53]. These centres are defined as the mean charge position in a system based on Wannier functions. This mathematical conceptualisation finds application in ν bands of a two-dimensional system, defined as follows [52, 53]

$$\psi_\nu = \frac{ia}{2\pi} \int_{-\pi/a}^{\pi/a} \langle \Upsilon_\nu(\mathbf{k}) | \nabla_{\mathbf{k}} | \Upsilon_\nu(\mathbf{k}) \rangle d\mathbf{k}. \quad (20)$$

It is evident that these WCCs are equivalent to the Berry phase calculation. However, in order to examine the topological evolution and extract information about the system, the WCCs must be calculated along k_x as a function of the transverse moment k_y , based on a modified form of equation (20)

$$\psi_\nu(k_y) = \frac{ia}{2\pi} \int_{-\pi/a}^{\pi/a} \langle \Upsilon_\nu(k) | \partial_{k_x} | \Upsilon_\nu(k) \rangle dk_x. \quad (21)$$

WCCs are calculated only for $k_y \in [0, 2\pi]$, signifying the displacement of the referential unit cell's center of charge along a closed trajectory of k_y . By varying the hopping energy for four cases ($\gamma_1 = 1\gamma, 1.5\gamma, 2.1\gamma$, and 2.5γ), it is observed that the WCC plots exhibit winding and discontinuity at the Dirac point as k_y increases, particularly in the standard case ($\gamma_1 = 1\gamma$), indicating a non-trivial topological phase of the system (see Fig. 7-(a)). However, when γ_1 surpasses 2γ , as illustrated in Fig. 7.(c)-(d), the movement of these centers suggests a transition from a non-trivial topological insulating state to a trivial topological state. This transition is characterized by the dissipation of the WCC windings, which become continuous and begin to oscillate around zero.

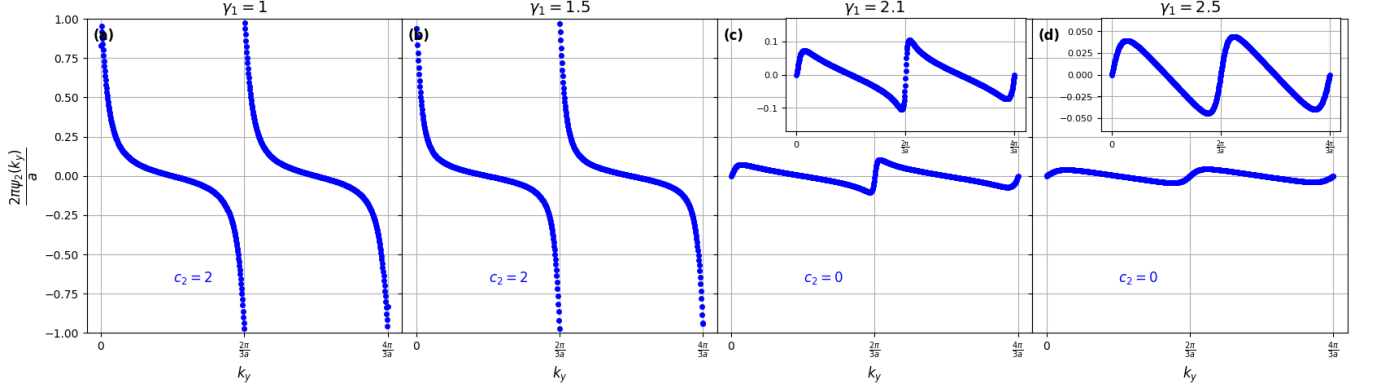


FIG. 7. Evolution of the Wannier charge center for the valence band ($\nu = 2$) along the x direction as a function of displacement k_y in the y direction. For (a) $\gamma_1 = 1\gamma$ and (b) $\gamma_1 = 1.5\gamma$, this evolution is characterized by a winding and discontinuity of the WCC at the Dirac points along k_y , when a closed cycle is traversed in the BZ, indicating a non-trivial topological phase. On the other hand, for (c) $\gamma_1 = 2.1\gamma$ and (d) $\gamma_1 = 2.5\gamma$, the winding of the WCCs disappears, the latter becoming continuous, meaning that the system is no longer in a topological insulating phase. The other parameters considered are $\alpha = 1$ and $\Delta = 0.18\gamma$.

V. ANOMALOUS HALL CONDUCTIVITY

In this section, we calculate and discuss the anomalous Hall conductivity (AHC) for the $\alpha - T_3$ lattice exposed to irradiation and deformation. This conductivity is evaluated by examining the electron response to an external electric field in an anisotropic context, providing information about the system topology. To determine the AHC, we integrate the Berry curvature over all occupied states in the entire Brillouin zone (BZ), by Eq.(16). We use the following formula to perform this calculation [54].

$$\sigma_{xy} = \frac{\sigma_0}{2\pi} \sum_{\nu} \int_{BZ} d^2k \Omega_{\nu}(\mathbf{k}) f_{\nu}(\mathbf{k}).$$

Where $f_{\nu}(\mathbf{k}) = [1 + e^{(\varepsilon_{\nu}(\mathbf{k}) - \mu)/k_B T}]^{-1}$ is the Fermi-Dirac distribution function, μ is the chemical potential, T is the temperature, k_B is the Boltzmann constant and $\sigma_0 = e^2/h$. The AHC can be calculated numerically as a function of the chemical potential μ at $T=100$ K by fixing $\Delta = 0.35\gamma$ and α for four cases: $\alpha = 0, 0.45, 0.8$ and 1 , while varying γ_1 , as shown in Fig.8.

We first examine the first two cases, $\alpha = 0$ and $\alpha = 1$, where the hopping energy γ_1 varies, as shown in Fig. 8(a) and (d). A quantised plateau is observed with $\sigma_{xy} = \sigma_0$ for $\alpha = 0$ and $\sigma_{xy} = 2\sigma_0$ for $\alpha = 1$. When the chemical potential μ lies within the global gap, the width of the plateau corresponds to that of the gap in the dispersion spectrum and increases proportionally with increasing Δ . It is noteworthy that σ_{xy} for $\alpha = 1$ is twice that for $\alpha = 0$. In this case, the Berry curvature associated with the flat band ($\nu = 1$) disappears and has no contribution to σ_{xy} . When μ intercepts the bands (whether conduction ε_0 or valence ε_2), σ_{xy} decreases. This decrease is explained by the fact that the integral is performed on occupied states and μ has left the global band.

In addition, the width of the plateau decreases with increasing γ_1 , as the overall gap between the dispersive bands narrows. At $\gamma_1 = 2\gamma$ the plateau disappears completely, as does the Hall conductivity.

For cases $\alpha \neq 0$ and 1 , the flat band ε_1 becomes dispersive, which changes the behaviour of the Hall conductivity. In fact, due to this dispersive nature, there is no longer a smooth plateau in the Hall conductivity. Instead, σ_{xy} exhibits a summit located at $\mu = 0$, as observed for $\alpha = 0.45$ (see Fig. 8(a)). In this scenario, two distinct plateaus of σ_{xy} are observed when μ lies within two energy gaps: one between the flat band ε_1 and ε_2 at point K, and the other between ε_0 and ε_1 at point K'. In these cases, the value of σ_{xy} for each plateau is $\sigma_{xy} = \sigma_0$.

For $\alpha = 0.8$, two similar plateaus are also observed, but the value of σ_{xy} reaches $\sigma_{xy} = 2\sigma_0$. This increase in σ_{xy} results from a phase transition when $\alpha = 1/\sqrt{2}$. As discussed earlier, the Chern number remains constant in the $1/\sqrt{2} < \alpha \leq 1$ phase, which keeps σ_{xy} at $2\sigma_0$. However, in this regime, there are no smooth plateaus in the Hall conductivity. Instead, σ_{xy} exhibits a dip near $\mu = 0$, as shown in Fig. 8(d).

Here, for $\alpha = 0.45$ and $\alpha = 0.8$, the width of the plateaus in σ_{xy} decreases with increasing γ_1 as long as $\gamma_1 < 2\gamma$ and disappears completely when $\gamma_1 \geq 2\gamma$.

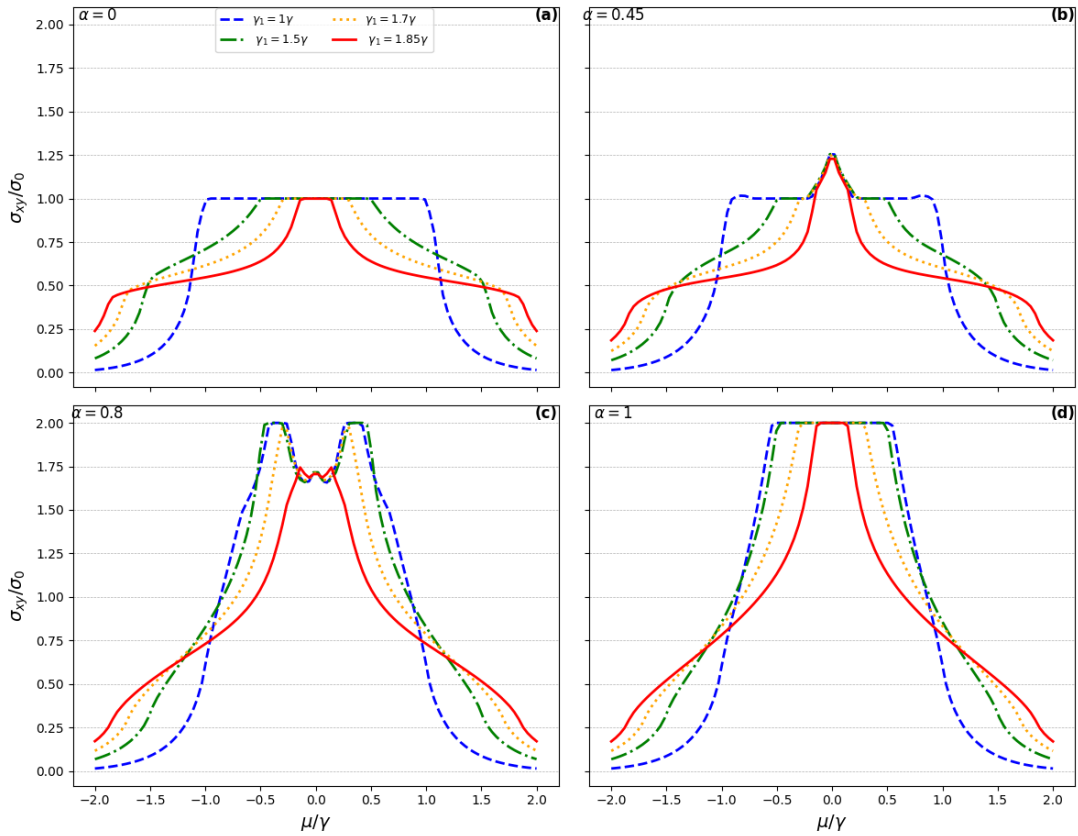


FIG. 8. Hall conductivity is depicted as a function of chemical potential μ for different values of γ_1 , as shown in the inset. The cases studied are (a) $\alpha = 0$, (b) $\alpha = 0.4$, (c) $\alpha = 0.8$ and (d) $\alpha = 1$.

Finally, we find that the value of α plays a crucial role in increasing the Hall conductivity as well as in widening the corresponding plateaus. These plateaus are proportional to the Chern number, with $\sigma_{xy} = |C_{0,2}|\sigma_0$ as long as the system remains a non-trivial topological insulator. However, these plateaus are sensitive to the hopping energy γ_1 , which leads to a progressive reduction in their width as γ_1 increases. Ultimately, these plateaus disappear when the band gap closes at the critical point $\gamma_1 = 2\gamma$, marking the system's transition to a trivial topological insulator state.

VI. CONCLUSION

In this work, we have investigated the effect of deformation on the topological properties induced by light polarisation in $\alpha - T_3$ lattices. We introduced this deformation by modifying the hopping energy in the $\alpha - T_3$ lattice, particularly by modifying γ_1 at the A-B and A-C sites along the δ_1 direction, while remaining unchanged hopping energies along the δ_2 and δ_3 directions. This modification of γ_1 led to a change in the band structure for three specific cases: $\alpha = 0$, $\alpha = 1/\sqrt{2}$ and $\alpha = 1$. In these cases, the Dirac cones at points \mathbf{K} and \mathbf{K}' move towards point \mathbf{M} when the system is subjected to off-resonance circular polarization. This polarisation induces a Haldane mass term at $\phi = \pi/2$, breaking the time-reversal symmetry. This term is responsible for the opening of a gap. However, in the case of $\alpha = 1/\sqrt{2}$, the gap partially opens at points \mathbf{K} and \mathbf{K}' . Moreover, the gap size decreases with increasing γ_1 and disappears completely when $\gamma_1 = 2\gamma$, where the system adopts semi-Dirac behaviour. This deformation, which breaks the C_3 symmetry, leads to a shift in the concentration of Berry curvature in the Brillouin zone, from points \mathbf{K} and \mathbf{K}' to point \mathbf{M} . In the standard case, $\gamma = \gamma_1$, we observe particle-hole symmetry for $\alpha = 0$ and $\alpha = 1$ and inversion symmetry. We have calculated the corresponding Chern numbers for the conduction (C_0), flat (C_1) and valence (C_2) bands: For $\alpha < 1/\sqrt{2}$ the Chern numbers are $C_0 = -1$, $C_1 = 0$ and $C_2 = 1$. For $\alpha \geq 1/\sqrt{2}$ the values change to $C_0 = -2$, $C_1 = 0$ and $C_2 = 2$. This shows a phase transition. We then focused on the Chern number corresponding to C_2 . Fixing $\alpha = 1$, we plotted C_2 as a function of γ_1 . It turned out that there is a phase transition with gap closure at $\gamma_1 = 2\gamma$. When $\gamma_1 > 2\gamma$, the system changes from a non-trivial topological insulator ($C_2 = 2$) to a trivial topological insulator ($C_2 = 0$). We have also plotted a phase diagram in the parameter space of Δ/γ and α by fixing

γ_1 . When $\gamma_1 = 2\gamma$, in the interval of Δ/γ_1 and α , the system transforms into a trivial topological insulator. This transition was confirmed by plotting the Wannier charge centre. Fixing γ_1 , we observed that the system changes state from a non-trivial topological insulator to another trivial topological insulator state when $\gamma_1 > 2\gamma$. We have also calculated the anomalous Hall conductivity for four values of α : 0, 0.45, 0.8, and 1. For $\alpha = 0$ and $\alpha = 0.45$, the conductivity shows quantized behaviour in the form of plateaus with a value of $\sigma_{xy} = 1\sigma_0$. For $\alpha = 0.8$ and $\alpha = 1$, the conductivity value increases to $\sigma_{xy} = 2\sigma_0$, characterized by a plateau at $\gamma_1 = \gamma$. This plateau decreases with increasing γ_1 and disappears when $\gamma_1 > 2\gamma$. These plateaus correspond to the Chern number, where $\sigma_{xy} = |C_{0,2}|\sigma_0$. The disappearance of these plateaus indicates that the system is transitioning from a non-trivial topological insulator to a trivial topological state.

ACKNOWLEDGEMENTS

The authors would like to acknowledge the " Hassan II Academy of Sciences and Technologies-Morocco for its financial support. The authors also thank the LPHE-MS, Faculty of Sciences, Mohammed V University in Rabat, Morocco for the technical support through facilities.

-
- [1] N. Bultinck, B. A. Bernevig, M. P. Zaletel, Three dimensional superconductors with hybrid higher-order topology, *Phys. Rev. B* 99 (2019) 125149.
 - [2] L. B. Drissi, S. Lounis, E. H. Saidi, Higher order topological matter and fractional chiral states, *The European Physical Journal Plus* 137, Article number: 796 (2022).
 - [3] Nagaosa, N., et Tokura, Y. (2013). Topological properties and dynamics of magnetic skyrmions. *Nature nanotechnology*, 8(12), 899-911.
 - [4] L. B. Drissi, E. H. Saidi, and M. Bousmina, Four-dimensional graphene. *Physical Review D*, 2011, vol. 84, no 1, p. 014504.
 - [5] C. C. Liu, W. Feng, Y. Yao, spin Hall effect in silicene and two-dimensional germanium. *Physical review letters*, 2011, vol. 107, no 7, p. 076802.
 - [6] L. B. Drissi, E. H. Saidi, Domain Walls in Topological Tri-hinge Matter, *European Physical Journal Plus* 136 (2021) 68.
 - [7] F. Schindler, A. M. Cook, M. G. Vergniory, Z. Wang, S. S. Parkin, B. A. Bernevig, and T. Neupert, Higher order topological insulators, *Science advances* 4 (2018) eaat0346.
 - [8] Hiromu Araki, Tomonari Mizoguchi, Yasuhiro Hatsugai, ZQ Berry Phase for Higher-Order Symmetry-Protected Topological Phases, *Phys. Rev. Research* 2 (2020) 012009.
 - [9] Klitzing, K. V., Dorda, G., et Pepper, M. (1980). New method for high-accuracy determination of the fine-structure constant based on quantized Hall resistance. *Physical review letters*, 45(6), 494.
 - [10] Thouless, D. J., Kohmoto, M., Nightingale, M. P., et den Nijs, M. (1982). Quantized Hall conductance in a two-dimensional periodic potential. *Physical review letters*, 49(6), 405.
 - [11] Laughlin, R. B. (1981). Quantized Hall conductivity in two dimensions. *Physical Review B*, 23(10), 5632.
 - [12] Fu, L., Kane, C. L., et Mele, E. J. (2007). Topological insulators in three dimensions. *Physical review letters*, 98(10), 106803.
 - [13] Haldane, F. D. M. (1988). Model for a quantum Hall effect without Landau levels: Condensed-matter realization of the "parity anomaly". *Physical review letters*, 61(18), 2015.
 - [14] Elbahri, A., Ragragui, M., Drissi, L.B., Saidi, E.H., Exploring topological phases in superconducting transition metal (Sc, Ti, V)-carbides, *Materials Science in Semiconductor Processing* 2025, 186, 108993.
 - [15] Zhang, D. W., Zhu, Y. Q., Zhao, Y. X., Yan, H., et Zhu, S. L. (2018). Topological quantum matter with cold atoms. *Advances in Physics*, 67(4), 253-402.
 - [16] Jiang, W., Kang, M., Huang, H., Xu, H., Low, T., et Liu, F. (2019). Topological band evolution between Lieb and kagome lattices. *Physical Review B*, 99(12), 125131.
 - [17] Kim, H. S., et Kee, H. Y. (2017). Realizing Haldane model in Fe-based honeycomb ferromagnetic insulators. *npj Quantum Materials*, 2(1), 20
 - [18] Lu, L., Joannopoulos, J. D., et Soljačić, M. (2014). Topological photonics. *Nature Photonics*, 8(11), 821-829.
 - [19] Zhang, X., Zangeneh-Nejad, F., Chen, Z. G., Lu, M. H., et Christensen, J. (2023). A second wave of topological phenomena in photonics and acoustics. *Nature*, 618(7966), 687-697.
 - [20] Li, S., Tian, R., Liu, M., Arzamasovs, M., Chen, L., et Liu, B. (2024). Topological flat band with higher winding number in a superradiance lattice. *Annals of Physics*, 471, 169837.
 - [21] Jacak, J. E. (2021). Topological approach to electron correlations at fractional quantum Hall effect. *Annals of Physics*, 430, 168493.
 - [22] Kane, C. L., et Mele, E. J. (2005). Z_2 topological order and the quantum spin Hall effect. *Physical review letters*, 95(14), 146802.
 - [23] Bentaibi, B., Drissi, L. B., Saidi, E. H., Bousmina, M., New room-temperature 2D hexagonal topological insulator OsC: First Principle Calculations, *Materials Science in Semiconductor Processing* 151 (2022) 107009.

- [24] Kou, L., Ma, Y., Sun, Z., Heine, T., et Chen, C. (2017). Two-dimensional topological insulators: Progress and prospects. *The journal of physical chemistry letters*, 8(8), 1905-1919.
- [25] Kitagawa, T., Oka, T., Brataas, A., Fu, L., et Demler, E. (2011). Transport properties of nonequilibrium systems under the application of light: Photoinduced quantum Hall insulators without Landau levels. *Physical Review B-Condensed Matter and Materials Physics*, 84(23), 235108.
- [26] McIver, J. W., Schulte, B., Stein, F. U., Matsuyama, T., Jotzu, G., Meier, G., et Cavalleri, A. (2020). Light-induced anomalous Hall effect in graphene. *Nature physics*, 16(1), 38-41.
- [27] Bao, C., Tang, P., Sun, D., et Zhou, S. (2022). Light-induced emergent phenomena in 2D materials and topological materials. *Nature Reviews Physics*, 4(1), 33-48.
- [28] Usaj, G., Perez-Piskunow, P. M., Foa Torres, L. E. F., et Balseiro, C. A. (2014). Irradiated graphene as a tunable Floquet topological insulator. *Physical Review B*, 90(11), 115423.
- [29] Ācenal, F. N., Seradjeh, B., et Eckardt, A. (2019). How to directly measure floquet topological invariants in optical lattices. *Physical Review Letters*, 122(25), 253601.
- [30] Nag, T., et Roy, B. (2021). Anomalous and normal dislocation modes in Floquet topological insulators. *Communications Physics*, 4(1), 157.
- [31] Skirlo, S. A., Lu, L., Igarashi, Y., Yan, Q., Joannopoulos, J., et Soljačić, M. (2015). Experimental observation of large Chern numbers in photonic crystals. *Physical Review Letters*, 115(25), 253901.
- [32] Dey, B., et Ghosh, T. K. (2019). Floquet topological phase transition in the $\alpha - T_3$ lattice. *Physical Review B*, 99(20), 205429.
- [33] Iurov, A., Zhemchuzhna, L., Gumbs, G., Huang, D., Fekete, P., Anwar, F., ... et Weekes, N. (2021). Tailoring plasmon excitations in $\alpha - T_3$ armchair nanoribbons. *Scientific reports*, 11(1), 20577.
- [34] Benhaida, O., Drissi, L. B., Saidi, E. H., et Laamara, R. A. (2024). Klein tunneling and Fabry-Perot resonances in the $\alpha - T_3$ bilayer with aligned stacking. *Physica Scripta*, 99(8), 085958.
- [35] Wang, J., et Liu, J. F. (2021). Quantum spin Hall phase transition in the $\alpha - T_3$ lattice. *Physical Review B*, 103(7), 075419.
- [36] Tamang, L., et Biswas, T. (2023). Probing topological signatures in an optically driven $\alpha - T_3$ lattice. *Physical Review B*, 107(8), 085408.
- [37] Dey, B., Kapri, P., Pal, O., et Ghosh, T. K. (2020). Unconventional phases in a Haldane model of dice lattice. *Physical Review B*, 101(23), 235406.
- [38] Parui, P., Ghosh, S., et Chittari, B. L. (2024). Topological properties of nearly flat bands in bilayer $\alpha - T_3$ lattice. *Physical Review B*, 109(16), 165118.
- [39] Benhaida, O., Saidi, E. H., Drissi, L. B., et Laamara, R. A. (2024). Topological Properties of Bilayer $\alpha - T_3$ Lattice Induced by Polarized Light. *arXiv preprint arXiv:2412.17763*.
- [40] Chen, W. C., Liu, R., Wang, Y. F., et Gong, C. D. (2012). Topological quantum phase transitions and topological flat bands on the star lattice. *Physical Review B* Condensed Matter and Materials Physics, 86(8), 085311.
- [41] Yang, S., Gu, Z. C., Sun, K., et Das Sarma, S. (2012). Topological flat band models with arbitrary Chern numbers. *Physical Review B* Condensed Matter and Materials Physics, 86(24), 241112.
- [42] Sticlet, D., et PiÅ©chon, F. (2013). Distant-neighbor hopping in graphene and Haldane models. *Physical Review B* Condensed Matter and Materials Physics, 87(11), 115402.
- [43] Mondal, S., et Basu, S. (2022). Vanishing of the quantum spin Hall phase in a semi-Dirac Kane-Mele model. *Physical Review B*, 105(23), 235409.
- [44] Alase, A., et Feder, D. L. (2021). Generating and detecting topological phases with higher Chern number. *Physical Review A*, 103(5), 053305.
- [45] Yang, Y., Li, X., et Xing, D. (2016). Topological phases and phase transitions on the honeycomb lattice. *The European Physical Journal B*, 89, 1-5.
- [46] Raoux, A., Morigi, M., Fuchs, J. N., PiÅ©chon, F., et Montambaux, G. (2014). From dia-to paramagnetic orbital susceptibility of massless fermions. *Physical review letters*, 112(2), 026402.
- [47] Lahiri, S., et Basu, S. (2024). Second order topology in a band engineered Chern insulator. *Scientific Reports*, 14(1), 1880.
- [48] Mondal, S., et Basu, S. (2023). Band-engineered bilayer Haldane model: Evidence of multiple topological phase transitions. *Physical Review B*, 108(4), 045307.
- [49] Mondal, S., et Basu, S. (2023). Topological features of the Haldane model on a dice lattice: Flat-band effect on transport properties. *Physical Review B*, 107(3), 035421.
- [50] Zhong, C., Chen, Y., Xie, Y., Sun, Y. Y., et Zhang, S. (2017). Semi-Dirac semimetal in silicene oxide. *Physical Chemistry Chemical Physics*, 19(5), 3820-3825.
- [51] Taherinejad, M., Garrity, K. F., et Vanderbilt, D. (2014). Wannier center sheets in topological insulators. *Physical Review B*, 89(11), 115102.
- [52] Gresch, D., Autes, G., Yazyev, O. V., Troyer, M., Vanderbilt, D., Bernevig, B. A., et Soluyanov, A. A. (2017). Z2Pack: Numerical implementation of hybrid Wannier centers for identifying topological materials. *Physical Review B*, 95(7), 075146.
- [53] Tyner, A. C. (2024). BerryEasy: a GPU enabled python package for diagnosis of nth-order and spin-resolved topology in the presence of fields and effects. *Journal of Physics: Condensed Matter*, 36(32), 325902.
- [54] Xiao, D., Chang, M. C., et Niu, Q. (2010). Berry phase effects on electronic properties. *Reviews of modern physics*, 82(3), 1959-2007.